Supplementary materials for "Long-range electron coherence in a Kagome metal"

Chunyu (Mark) Guo[†],[1] Kaize Wang,[1] Ling Zhang,[1] Carsten Putzke,[1] Dong Chen,[2,3] Maarten R. van Delft,[4,5] Steffen Wiedmann,[4,5] Fedor F. Balakirev,[6] Ross McDonald,[6] Martin Gutierrez-Amigo,[7] Manex Alkorta,[8,9] Ion Errea,[8,10,11] Maia G. Vergniory,[10,2] Takashi Oka,[12] Roderich Moessner,[13] Mark H. Fischer,[14] Titus Neupert,[14] Claudia Felser,[2] and Philip J. W. Moll[†1]

[1]*Max Planck Institute for the Structure and Dynamics of Matter, Hamburg, Germany*

[2]*Max Planck Institute for Chemical Physics of Solids, Dresden, Germany*

[3]*College of Physics, Qingdao University, Qingdao, China*

[4]*High Field Magnet Laboratory (HFML - EMFL), Radboud University, Toernooiveld 7, 6525 ED Nijmegen, The Netherlands*

[5]*Radboud University, Institute for Molecules and Materials, Nijmegen 6525 AJ, Netherlands*

[6]*National High Magnetic Field Laboratory, Los Alamos National Laboratory, Los Alamos, New Mexico 87545, USA*

[7]*Department of Applied Physics, Aalto University School of Science, FI-00076 Aalto, Finland*

[8]*Centro de Física de Materiales (CSIC-UPV/EHU), Donostia-San Sebastian, Spain*

[9]*Department of Physics, University of the Basque Country (UPV/EHU), Bilbao, Spain*

[10]*Donostia International Physics Center, Donostia-San Sebastian, Spain*

[11]*Fisika Aplikatua Saila, Gipuzkoako Ingeniaritza Eskola, University of the Basque Country (UPV/EHU), Donostia-San Sebastian, Spain*

[12]*The Institute for Solid State Physics, The University of Tokyo, Kashiwa, Japan*

[13]*Max Planck Institute for the Physics of Complex Systems, Dresden, Germany*

[14]*Department of Physics, University of Zürich, Zürich, Switzerland*

(Dated: March 31, 2025)

†Corresponding authors: chunyu.guo@mpsd.mpg.de(C.G.); philip.moll@mpsd.mpg.de(P.J.W.M.).

A. Crystal synthesis and device fabrication

Plate-like single crystals of CsV_3Sb_5 are obtained following a self-flux procedure as described in Ref.[1]. They crystallize in the hexagonal structure (P6/mmm space group). The micro-devices (S1 to S8) are fabricated using the focused-ion-beam (FIB) technique (Fig. S 1). The microstructure fabrication procedure and the initial test on device quality are performed following the previously reported recipe[2,3]. A slab of the bulk material (lamella) is dug out and transferred in situ by a micro-manipulator and welded to a gold-coated (Au:300 nm) SiN_x membrane chip via Pt-deposition with ion beams. To clarify the influence of FIB-deposited contacting electrodes, device S3 is gold-coated after the lamella transfer process. The membrane window is later carved into meander-shaped springs, which become the only mechanical connections from the device to the supporting substrate. These soft springs with low spring constant $\approx$ 150 N/m significantly reduce the thermal contraction strain. The lamella is then fabricated into the desired shape following a low-voltage (2 kV) and low-current (100 pA) Xe ion beam cleaning as the final fabrication step to reduce the thickness of the FIB-damaged amorphous layer. To reduce the torque force at high magnetic fields, devices S3 and S5 are attached rigidly on one side of the silicon substrate with Pt-deposition, and the clear consistency among all devices demonstrates the irrelevance of the magnetic torque effect in our measurements.

B. Electrical measurements

Resistance measurements were performed using a multichannel Synktek lockin in a Dynacool PPMS system with a maximal magnetic field of 14 T. A low AC current of 30 μA is used to measure all devices to avoid Joule heating. The absence of notable self-heating has been confirmed by the absence of higher harmonic responses. The consistent observation of clear Shubnikov–de Haas oscillations and high electric conductivity at low temperatures demonstrates the intact physical properties of all FIB-fabricated devices and the irrelevance of the FIB-damaged amorphous layer, which typically encases the samples with a thickness of 10 nm corresponding to a negligible fraction of the sample cross-section. The field dependence of magnetoresistance at base temperature (T = 2 K) shows a slight variation across different devices (Fig. S 2), mainly at-

tributed to a small misalignment between the magnetic field direction and the Kagome plane. The subtracted second derivative demonstrates a consistent oscillation frequency change with varying sample width following the description of h/e oscillations. For an estimation of uncertainty, we fit the width (w) dependence of the oscillation period (ΔB) based on the relation: $\Phi_0 = \Delta B w c'$. This yields $c' = 9.11 \pm 0.36$ Å, which is near identical to the c-axis lattice parameter in CsV_3Sb_5 ($c = 9.28$ Å). The errors of this analysis are mainly attributed to the uncertainty in determining the exact oscillation period ΔB.

C. Subtraction of oscillations: polynomial fitting versus second-order derivative

Two independent methods have been used to remove the background of magnetoresistance to check the consistency of the h/e oscillations subtracted (Fig. S 3). These methods follow the common practices of the analysis of SdH oscillations. First, we directly take the second-order derivative of the field dependence of the magnetoresistance, and the periodic-in-field oscillations are readily observable. When the magnetoresistance possesses a continuously varying second-order derivative, the resulting background may mask the oscillatory part of the signal. For the complimentary analysis, the MR is fitted with a 5th-order polynomial, and the subtracted part displays consistent oscillatory behavior. The polynomial was checked to ensure that it did not contain notable oscillatory behavior and did not introduce artificial oscillations into the data. This way, the background is subtracted further, while its direct comparison to the second-order derivative reveals a one-to-one correspondence with the pi-phase shift. It clearly demonstrates the consistency between these methods in analyzing h/e oscillations. All raw data, as well as the background-subtracted data, are made available in the online repository.

D. Influence of strain effect

The electronic response in CsV_3Sb_5 is extremely sensitive to the influence of strain effect, as consistently demonstrated by previous observations[2,3]. To explore the possible strain-sensitivity of h/e oscillations, we mounted the device directly to a sapphire substrate without the membrane springs for mechanical buffering (Fig. S 4). The mismatch of the thermal expansion coefficient between the device and the sapphire substrate leads to a tensile strain on the device which reaches $\sim 0.3\%$ at $T = 2$ K[3]. Its impact is elaborated by the clear increase of the charge ordering tempera-

ture, while the broadening of the transition is due to the unavoidable strain inhomogeneity across the microstructure. Importantly, the h/e oscillations are strongly suppressed in the strained device. Its comparison to a nearly strain-free device (S6) with a similar sample width demonstrates more than 90% reduction of oscillation amplitude due to strain. Moreover, the oscillation disappears quickly with increasing field as only the first period can be clearly resolved. Given the actual change of lattice parameter due to tensile strain is less than 0.5%, the deconstructive interference caused by the inhomogeneous lattice constant across the strained device cannot be the main source of the reduction observed. In contrast, it aligns with the observed suppression of strain in magneto-chiral transport signatures[2]. This indicates a fundamental link between long-range coherence and correlated electronic order in CsV_3Sb_5.

E. Transport mean free path analysis

The transport mean free path l_t denotes the distance an excited quasiparticle travels before its momentum has been randomized by scattering. The idea is based on the decay time of a DC transport current when the driving DC electric field is instantaneously removed at some point in time. Scattering processes with the lattice and its defects will transfer momentum from the electron system and eventually bring it to rest, leading to a characteristic current decay $I(t) = I_0 e^{-t/\tau_t}$. This transport lifetime τ_t can be translated to a mean distance between scattering events of a quasiparticle at the speed of the Fermi velocity v_F simply via $l_t = v_F \tau_t$, which can be related to conductivities via Boltzmann transport. Such a picture of freely traveling quasiparticles between scattering events is critical in mesoscopic physics when device sizes are similar to this mean distance between scattering. However, this simple logic only rigorously works in simple cases, in particular in isotropic metals (spherical Fermi surface) with only one single band and carrier type. For complex multi-band metals hosting both electrons and holes on Fermi surface sheets with non-spherical shapes, this assumption is not generally valid. Scattering processes are momentum- and band-dependent, and a global decay time cannot be assumed to reflect directly onto each individual electron state. On top, the strong electron-phonon coupling results in non-trivial momentum dependences of the scattering matrix elements via the phonon-dispersion. As a result, the question of ballistic transport in such materials, in practice, is challenging. The goal is to apply the simplest analysis and show its mean free path to fall substantially below the device size, hence speaking against ballistic transport.

We start by estimating the transport mean free path based on the Drude model:

$$\sigma_{xx} = ne^2\tau/m^* \tag{S1}$$

The conductivity is directly obtained from the measurements of in-plane resistivity of device S5. The carrier density is extracted from the previous report of Hall voltage measurements on CsV_3Sb_5[4]. At T = 5 K, the hall resistivity ρ_{xy} reaches 0.47 $\mu\Omega$ cm at B = 14 T. Given the almost linear-in-field ρ_{xy}, the carrier density n is estimated to be $\approx$ 1.86 x 10^{22} cm^{-3} under the assumption of single conduction band. For simplicity, we also assume that the carrier density is temperature-independent, as the temperature variation of Hall resistivity is mainly attributed to the evolution of carrier mobilities of different pockets while the electronic structure remains almost intact below 50 K. Since the Brillouin zone is majorly occupied by the hexagonal Fermi surface, the in-plane Fermi wavevector can be estimated by: $n = \frac{3\sqrt{3}}{2}k_{F,x}^2 k_{F,z}/4\pi^3$ with $k_{F,z}$ directly determined by the lattice constant $c \approx 9$ Å ($k_{F,z} = 2\pi/c$). Therefore, the transport mean free path can be calculated by:

$$l_t = v_F\tau = \frac{\hbar k_{F,x}\sigma}{ne^2} = \frac{\hbar\sigma}{e^2\sqrt{0.1316n/c}} \tag{S2}$$

which allows us to extract the transport mean free path directly from the temperature dependence of resistivity (Fig. S 5). Right above the superconducting transition temperature (T_c = 2.8 K), the transport mean free path reaches 500 nm and then quickly drops to 150 nm as the temperature increases to 20 K. These values are well below the characteristic sizes of all devices measured.

As stated above, this estimate is based on crude approximations. Firstly, due to the slightly non-linear field dependence of Hall resistivity, the single-band assumption may lead to an under-estimation of the total carrier count across multiple conduction bands. Secondly, the assumption of a singular, hexagonal 2D Fermi surface oversimplifies the complex Fermiology in CsV_3Sb_5, which affects the approximation of the Fermi wavelength based on carrier density. As the single-band assumption tends to overestimate the averaged Fermi velocity, these estimations are rather an upper bound for the transport mean free path l_t. Given the aforementioned difficulties, one may still argue for substantially suppressed scattering for some regions of one of the Fermi surfaces to reach a quasi-ballistic limit for these few select states only. However, this would imply an extreme variation of lifetime across the Fermi surface, a highly unusual feature of materials dominated by impurity scattering.

This further supports our conclusion that the sizes of the microstructures we studied are all substantially larger than l_t, especially at elevated temperatures.

F. Dingle analysis for subtracting quantum mean free path

The quantum mean free path is obtained by analyzing the field dependence of the SdH oscillation amplitude measured with the magnetic field applied along the c-direction (Fig. S 6). According to the Lifshitz-Kosevich model, the oscillations can be described as[5]:

$$\Delta\rho_{\parallel}/\rho_{\parallel}^{0} \propto \sqrt{B}\sum_{r=1}^{\infty}\frac{R_D^r R_T^r}{r^{1/2}}\cos(r\lambda)\cos\left[r\left(2\pi\frac{F_0}{B}+\pi\right)+\phi_{LK}\right]. \tag{S3}$$

The oscillation amplitude can be smeared due to the finite quasiparticle lifetime τ and nonzero temperature T, which result in the well-known Dingle amplitude factor and thermal damping factor, respectively:

$$R_D^r := \exp\left(-\frac{r}{2}\frac{h}{\varepsilon_c\tau_q}\right), \quad R_T^r := \frac{a_r}{\sinh(a_r)}, \quad a_r := \frac{2\pi^2 r k_B T}{\varepsilon_c}, \tag{S4}$$

with $\varepsilon_c = \hbar|eB|/m_c$ the cyclotron energy, $m_c = (2\pi)^{-1}\partial S/\partial E$ the cyclotron mass, and τ_q the quantum lifetime. We first determine m_c via the temperature dependence of oscillation amplitude (Fig. S 6b), while the exponential growth of oscillation amplitude with increasing magnetic field stands for the enlarging ratio between the cyclotron energy and the Landau level broadening due to scattering events and therefore can be used to obtain the quantum lifetime. The relation between the field dependence of quantum oscillation amplitude and quantum life time τ_q can expressed as:

$$f(B^{-1}) = \ln[Amp\sqrt{B}\sinh(14.69m_cT/B)] = -\frac{\pi m_c}{e\tau_q}B^{-1} + Const. \tag{S5}$$

by extracting the linear slope of the $f(B^{-1})$(Fig. S 7), τ_q can be obtained. Its inaccuracy is determined by the uncertainty of the linear fitting (see error bars in Fig. 2). The calculation of the quantum mean free path, $l_q = v_F\tau_q$, further requires the value of Fermi velocity v_F, which can be directly calculated with the oscillation frequency and cyclotron mass:

$$v_F = \frac{\hbar k_F}{m_c} = \frac{\sqrt{2\hbar eF}}{m_c} \tag{S6}$$

This allows us to determine the temperature dependence of l_q for both the γ and δ pockets as shown in Fig.2.

G. Comparison between h/e oscillations and chiral transport

As illustrated in Fig.2b, the amplitude of the h/e oscillations is strongly suppressed when the magnetic field is rotated away from the in-plane direction. Such a distinct angular dependence

directly corresponds to the magneto-chiral transport as previously observed[2]. The absolute value of the second harmonic voltage $V_{2\omega}$ signal, which stands for the non-reciprocal transport signature in CsV_3Sb_5, displays an identical angular dependence with the h/e oscillations (Fig. S 8). This striking correspondence is consistently observed in both devices S2 and S4, suggesting the significant modulation of electronic orders in CsV_3Sb_5 and the possible role of quantum phase coherence in the appearance of the chiral-magneto transport.

H. Simulation of semiclassical Bloch-Lorentz oscillations

Here, we present the formalism for the semiclassical B-periodic oscillation as shown in Fig.2b. We use the Boltzmann transport equation(BTE) to calculate the magneto-conductivity σ_{zz} along c-axis of finite-size quasi-two-dimensional materials as shown in (Fig. S 8).

For quasi-two-dimensional materials, the band dispersion is modeled by

$$\varepsilon(\mathbf{k}) = \varepsilon_{\parallel}(\mathbf{k}_{\parallel}) - t_z \cos(k_z d), \tag{S7}$$

where $\mathbf{k}_{\parallel} = (k_x, k_y)$ is the in-plane momentum and d is the interlayer distance. The out-of-plane coupling t_z is assumed to be weak, i.e., t_z is much smaller than the bandwidth given by $\varepsilon_{\parallel}$.

We use linearized ansatz for the distribution function $f(\mathbf{r}, \mathbf{k})$,

$$f(\mathbf{r}, \mathbf{k}) = f^0 - \frac{\partial f^0}{\partial \varepsilon} h(\mathbf{r}, \mathbf{k}), \tag{S8}$$

where f^0 is the Fermi-Dirac distribution function.

Assuming we impose an electric filed $\mathcal{E}_z$ in the z-direction, the BTE under relaxation time approximation reads

$$\mathbf{v}(\mathbf{k}) \cdot \nabla_{\mathbf{r}} h - \frac{e}{\hbar}[\mathbf{v}(\mathbf{k}) \times \mathbf{B}] \cdot \nabla_{\mathbf{k}} h - e v_z(k_z) \mathcal{E}_z = -\frac{h(\mathbf{r}, \mathbf{k})}{\tau}, \tag{S9}$$

where $\mathbf{v}(k) = \partial\varepsilon(\mathbf{k})/\partial\mathbf{k}$ is Fermi velocity vector and $\mathbf{B} \equiv B(\cos\theta\cos\varphi, \cos\theta\sin\varphi, \sin\theta)$ is external magnetic field.

For a finite-size sample with length L and width w, we impose a completely diffusive boundary condition,

$$h(\mathbf{r}_B, \mathbf{k}_{\parallel}, k_z) = 0 \qquad \mathbf{v}(\mathbf{k}_{\parallel}) \cdot \hat{\mathbf{n}}_B < 0, \tag{S10}$$

where $\mathbf{r}_B$ is arbitrary position vector at the boundary and $\hat{\mathbf{n}}_B$ is the norm vector at $\mathbf{r}_B$.

With this boundary condition, the distribution function $h(\mathbf{r}, \mathbf{k})$ can be exactly solved by the method of characteristics[6,7]. Therefore, the conductivity can be calculated as

$$\sigma_{zz} = \frac{e}{S_{\|}\mathcal{E}_z} \int_{S_{\|}} d^2\mathbf{r}_{\|} \int_{\mathrm{BZ}} \delta(\varepsilon - \varepsilon_F) h(\mathbf{r}, \mathbf{k}) v_z(\mathbf{k}) d^3k \tag{S11}$$

For an out-of-plane magnetic field with moderate tilting angle θ up to 30°, we use an isotropic dispersion $\varepsilon_{\|}(\mathbf{k}_{\|}) = {\mathbf{k}_{\|}}^2/2m^*$ to model the in-plane dispersion. The solution gives rise to B-periodic oscillation of the conductivity as shown in (Fig. S 9). The physical reason for this is that when the oscillation period is commensurate with the sample width, all the semiclassical trajectories have a zero net z-direction displacement over the time of flight. Resulting in a minimal at every commensurate field[6]. Since a moderate tilting angle θ does not change the in-plane trajectory drastically, the commensurate condition still holds except for a pre-factor $\cos\theta$ due to projection. Thus, the semiclassical B-period oscillation can be observed over a large window of out-of-plane angle φ as shown in Fig. 2b.

We also present the result of varying φ at $\theta = 0^\circ$ for the in-plane magnetic field. We try two different models for the in-plane dispersion $\varepsilon_{\|}$: cylindrical and hexagonal models (Fig. S 10). Surprisingly, the oscillation vanishes quickly for a cylindrical Fermi surface when rotating away from the principal axis. On the other hand, the oscillation remains visible when rotating to a larger angle in the case of a hexagonal Fermi surface. Yet, multiple oscillation frequencies coexist due to the three dominant directions of Fermi velocities. Therefore the simulation in both limiting cases cannot capture the experimental signatures even qualitatively, in particular regarding the angular dependence.

I. Consistent switch at 45 degrees

To investigate the universality of the switching behavior illustrated in Fig. 3, we measured the angular dependence of oscillation periodicity in two microstructures, S1 and S4. Devices S1 and S4 have significantly different dimensions at their cross-sections. Device S1 features a narrow channel, with its width being nearly half its depth and, therefore, distinct oscillation periods and amplitudes with field applied either parallel or perpendicular to the crystalline a-direction (Fig. S 11a-d). Meanwhile, such a difference is much less significant in S4 due to its comparable width and depth (Fig. S 11e-g). Despite their distinction in dimensions, the periodicity switch at 45 degrees modulo 90 degrees was consistently observed in both samples (Fig. S 12), emphasizing

the irrelevance of the device geometry and its close connection to the correlated electronic order.

J. Temperature dependence across various devices

As microstructures vary in size, the reduction of h/e oscillation amplitude with increasing temperature behaves differently across various devices. Reducing the device's width shifts the onset of the oscillations, defined by the temperature where the oscillation amplitude gets larger than 5% of the amplitude at T = 2 K, up to a higher temperature (Fig. S 13). By linearly extrapolating to zero width, the onset temperature is determined to be about 33 K, which coincides with the T' as explained. It is much higher than the onset of quantum oscillations in CsV_3Sb_5 (Fig. S 6), which displays no variation across all devices of different sizes.

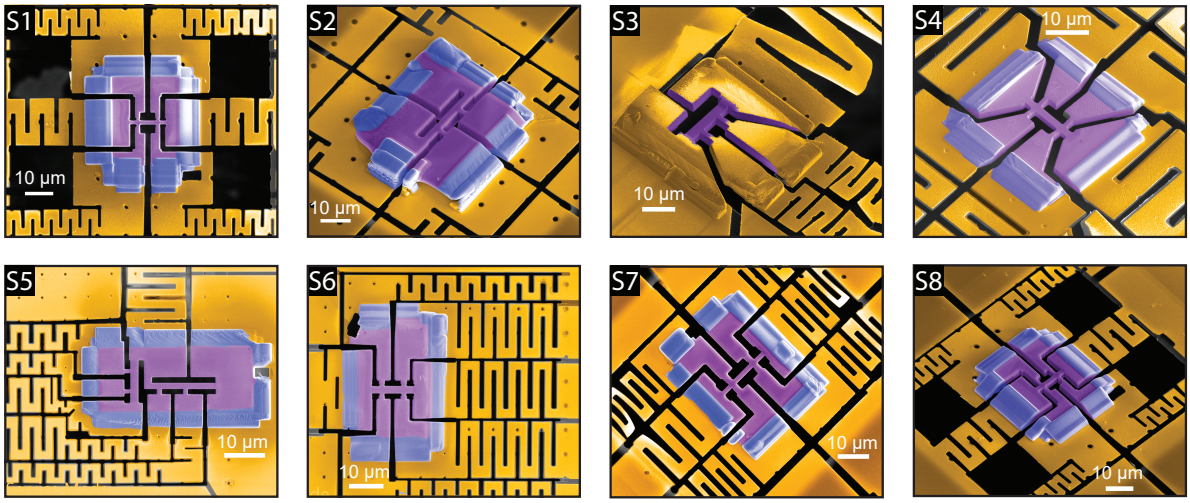

Fig. S 1. **Scanning electron microscope (SEM) images of all devices.** All microstructures utilize the soft membrane springs to reduce the thermal differential strain effect at low temperatures.

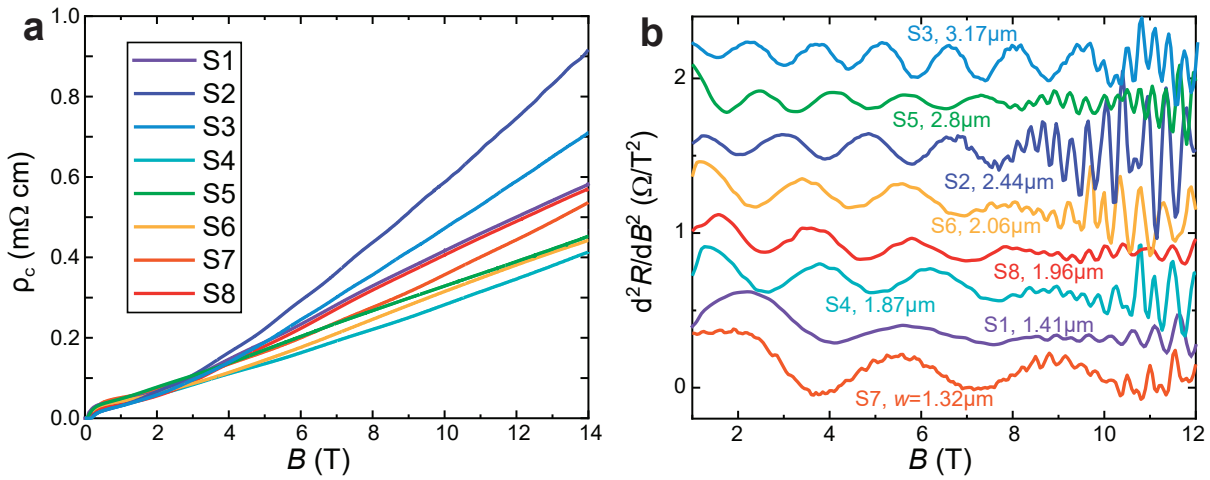

Fig. S 2. **Summary of all magnetoresistance and corresponding h/e oscillations.** (a) The magnetoresistance of all devices increases monotonically with increasing field, and the difference between their values is mainly attributed to the inevitable misalignment between the magnetic field and crystalline a-direction. (b) The second derivative of the field-dependent magnetoresistance clearly reveals the presence of h/e oscillations in all devices. Note that each curve is shifted by at least 0.3 Ω/T^2 for clarity.

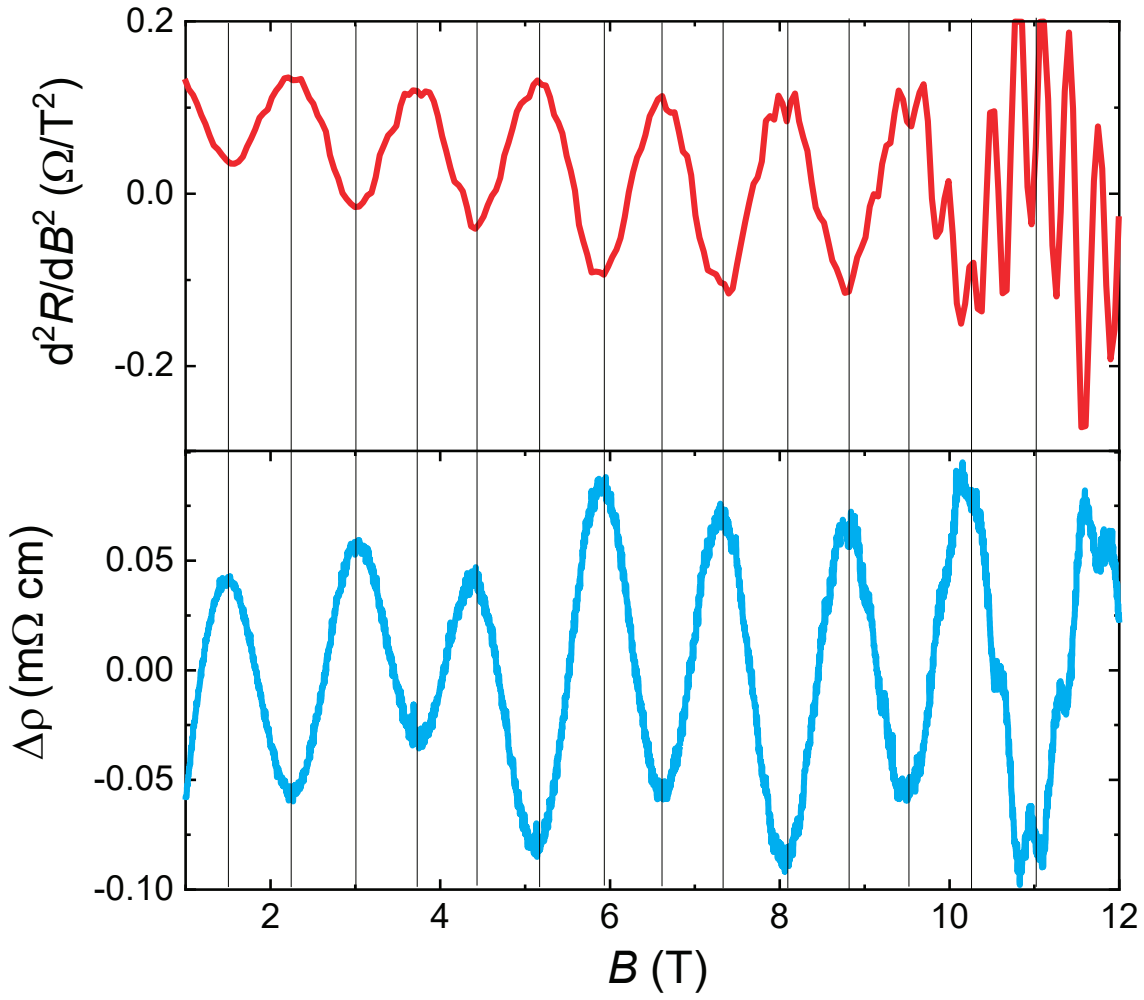

Fig. S 3. **Comparison of h/e oscillations subtracted by two different methods.** The h/e oscillations can be clearly resolved by either taking the second field derivative or subtracting the 5th-polynomial fitting as a background. The main difference between these two methods is a π-phase shift, as demonstrated by the flipped peak-valley correspondence between them.

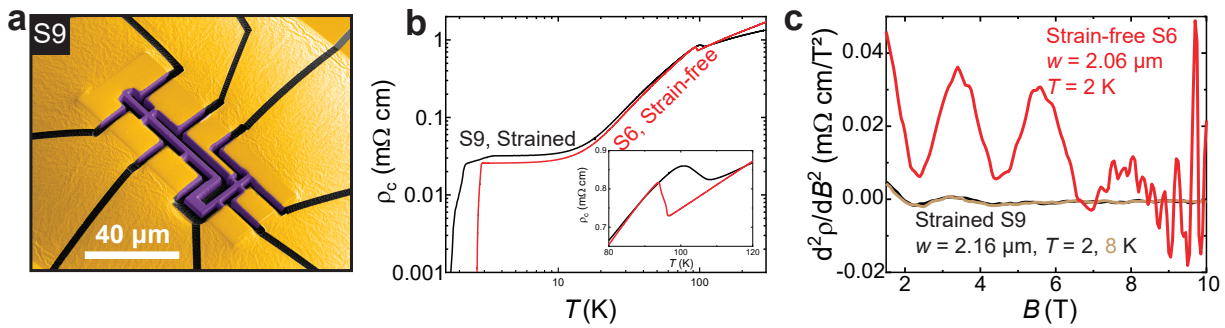

Fig. S 4. **Influence of uniaxial strain.** (a) SEM image of device S9. The device is mechanically attached to a sapphire substrate with via a double-component glue droplet. At low temperatures, the thermal expansion coefficient mismatch between the device and the substrate results in a substantial uniaxial strain across the device. (b) T-dependent resistivity of strained and nearly strain-free devices. Due to the presence of tensile strain, the charge order temperature is clearly increased, and its broadening is possibly attributed to the strain inhomogeneity. (c) Comparison of h/e oscillations in both devices. The oscillations are strongly suppressed in the strained device and only one oscillation period is visible. This is expected given the extraordinarily strain-sensitivity of CsV_3Sb_5 as consistently demonstrated in previous works[2,3].

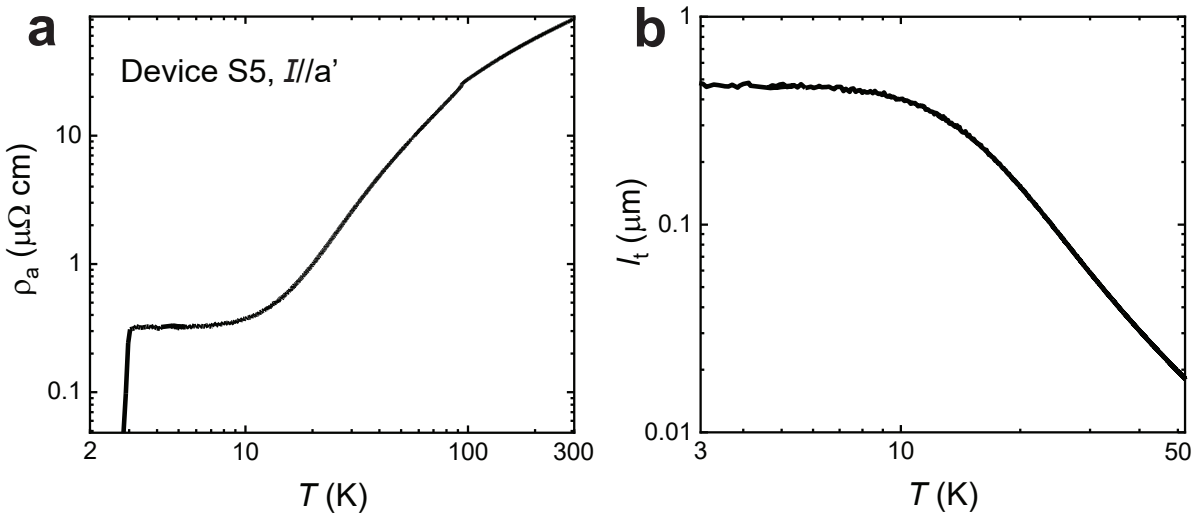

Fig. S 5. **Transport mean free path extracted from Drude model.** (a) In-plane resistivity measured with current applied perpendicular to the a-direction. The kink at 94 K stands for the charge-density-wave transition, while the superconducting transition is at T_c = 2.8 K. Both values agree well with the previous report on bulk samples[1,8], demonstrating the unchanged device properties after FIB-fabrication. (b) Transport mean free path estimated from the in-plane resistivity based on the Drude model.

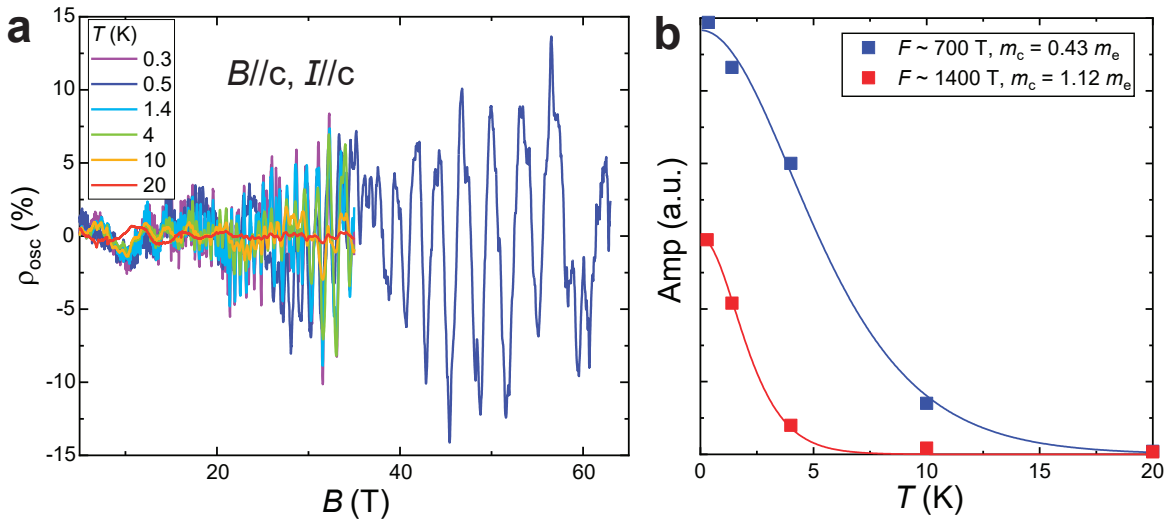

Fig. S 6. **Quantum oscillations and cyclotron mass analysis.** (a) Quantum oscillations at various temperatures. The oscillations are obtained from the magnetoresistance by subtracting a 5th-order polynomial fitting as a background. The measurement at T = 0.5 K is performed in a pulsed magnet up to 63 T, while others are measured in a water-cooled static magnet up to 35 T. (b) Lifshitz-Kosevich fitting to the temperature dependence of oscillation amplitudes determines the cyclotron masses of two main Fermi pockets in CsV_3Sb_5.

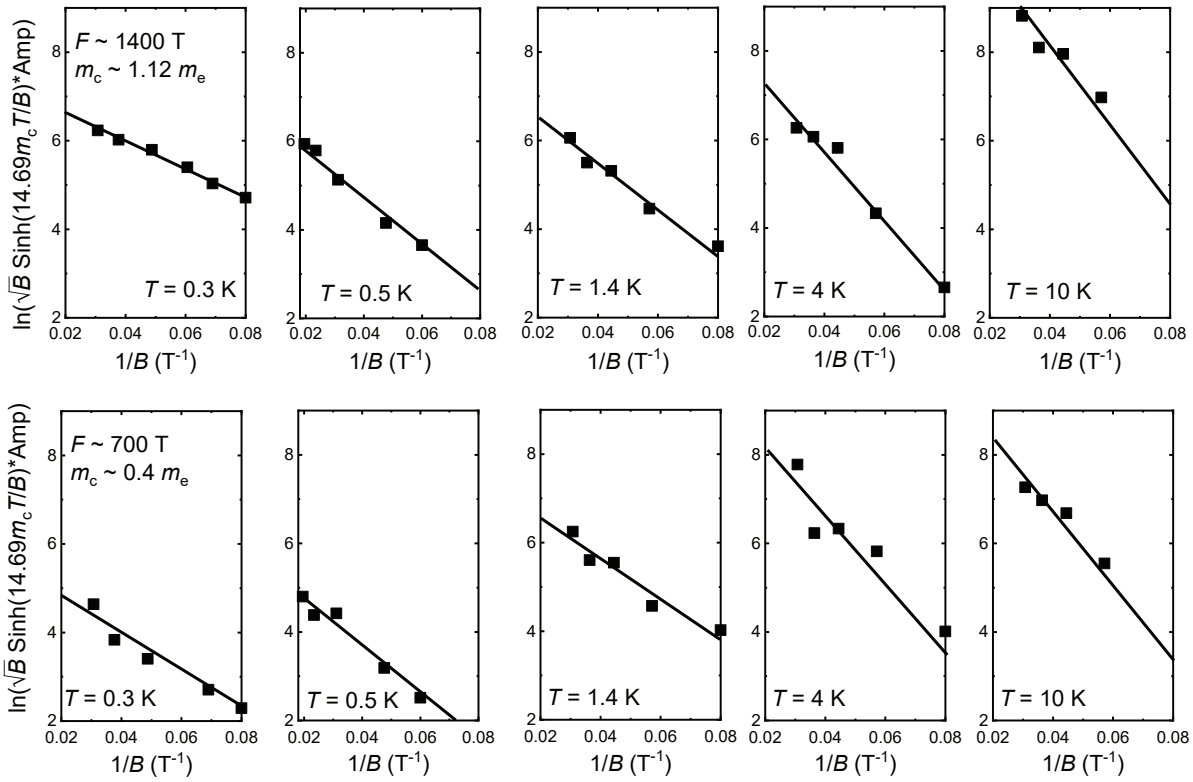

Fig. S 7. **Quantum mean free path extracted from Dingle analysis.** Extrapolation of field-dependent oscillation amplitude yields the quantum lifetime for each Fermi surface at various temperatures. The linear fitting coefficient leads to the determination of the quantum mean free path as presented in Fig. 2a.

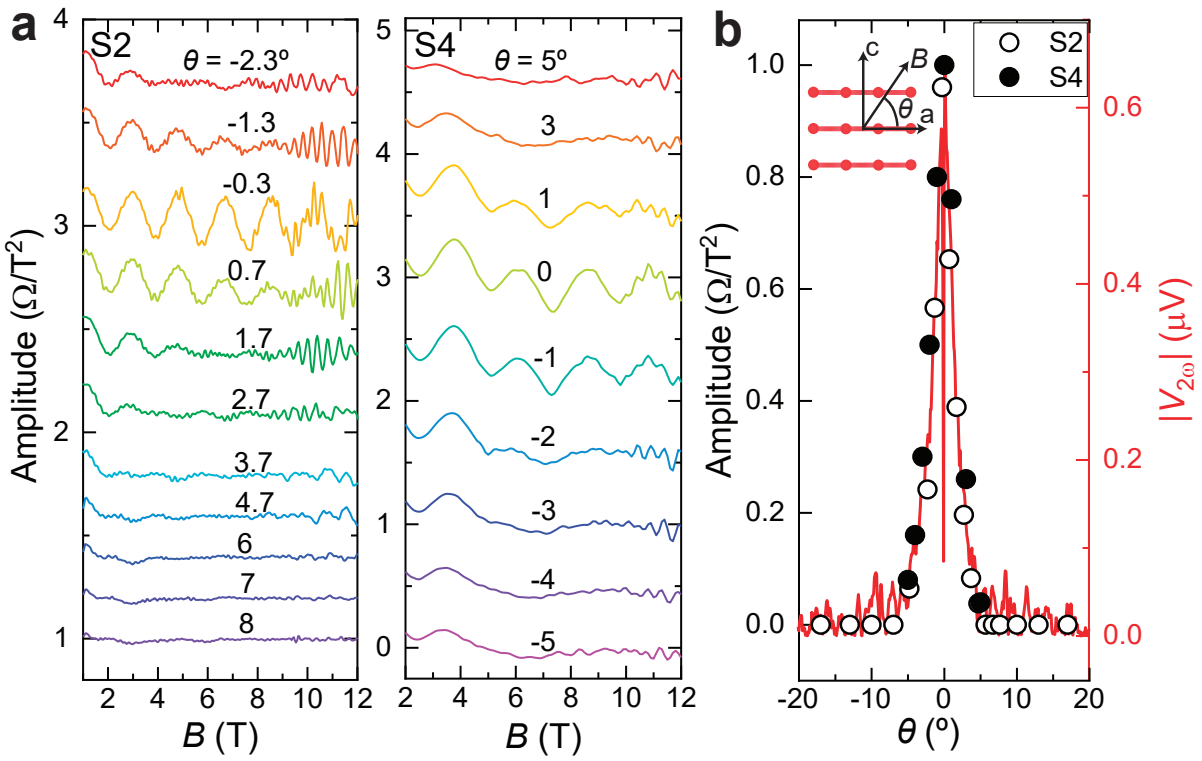

Fig. S 8. **Identical angular dependence of chiral magneto transport and h/e oscillations.** (a) h/e oscillations measured at different out-of-plane angle θ for both device S2 and S4. The oscillation becomes almost invisible at angles larger than 5°. (b) Comparison between h/e oscillations and the non-reciprocal transport signature $V_{2\omega}$[2]. Their identical angular dependence suggests the close relation between them.

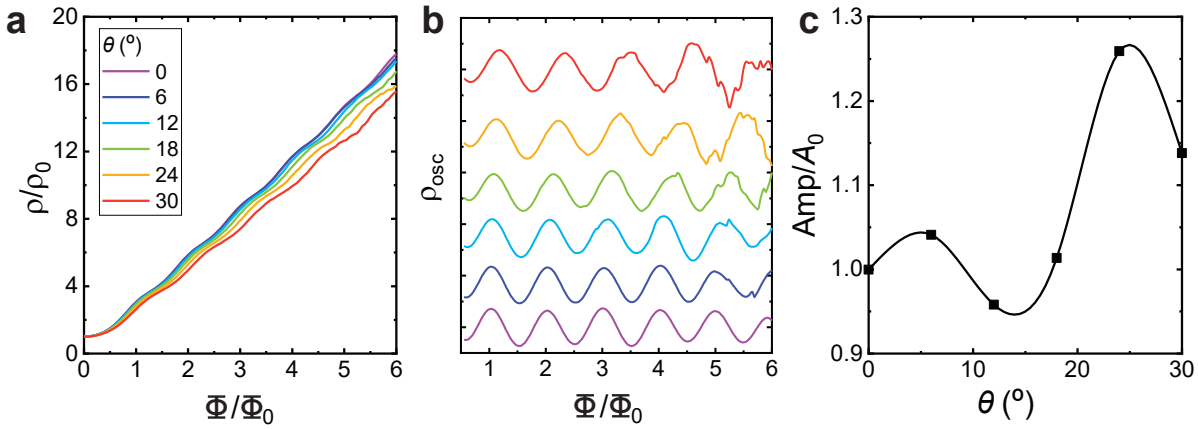

Fig. S 9. **Angular dependence of simulated Bloch-Lorentz oscillations based on a cylindrical Fermi surface.** (a) and (b) stands for the simulated magnetoresistance and Bloch-Lorentz oscillations, respectively. With the magnetic field rotated from in-plane to out-of-plane direction, the oscillation amplitude merely changes slightly, as shown in (c), which is distinct from the experimental observations.

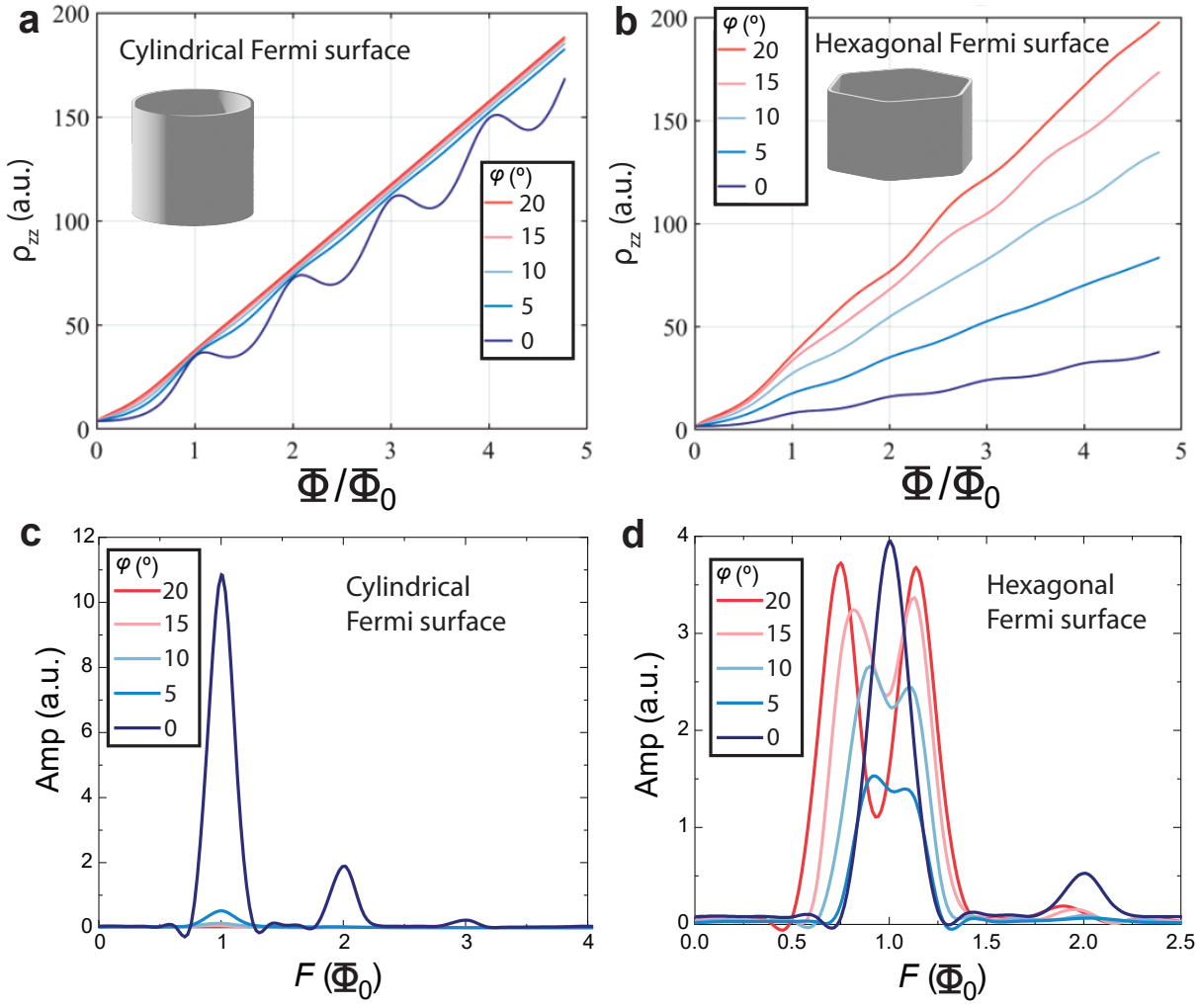

Fig. S 10. **Comparison between cylindrical and hexagonal Fermi surface.** (a) and (b) stands for the Bloch-Lorentz oscillation simulation for cylindrical and hexagonal Fermi surfaces respectively, while (c) and (d) present the FFT analysis of the oscillatory parts in both cases. With the magnetic field rotated in-plane, the oscillation amplitude varies quickly in the case of cylindrical Fermi surface, while its change in the hexagonal case is not as significant.

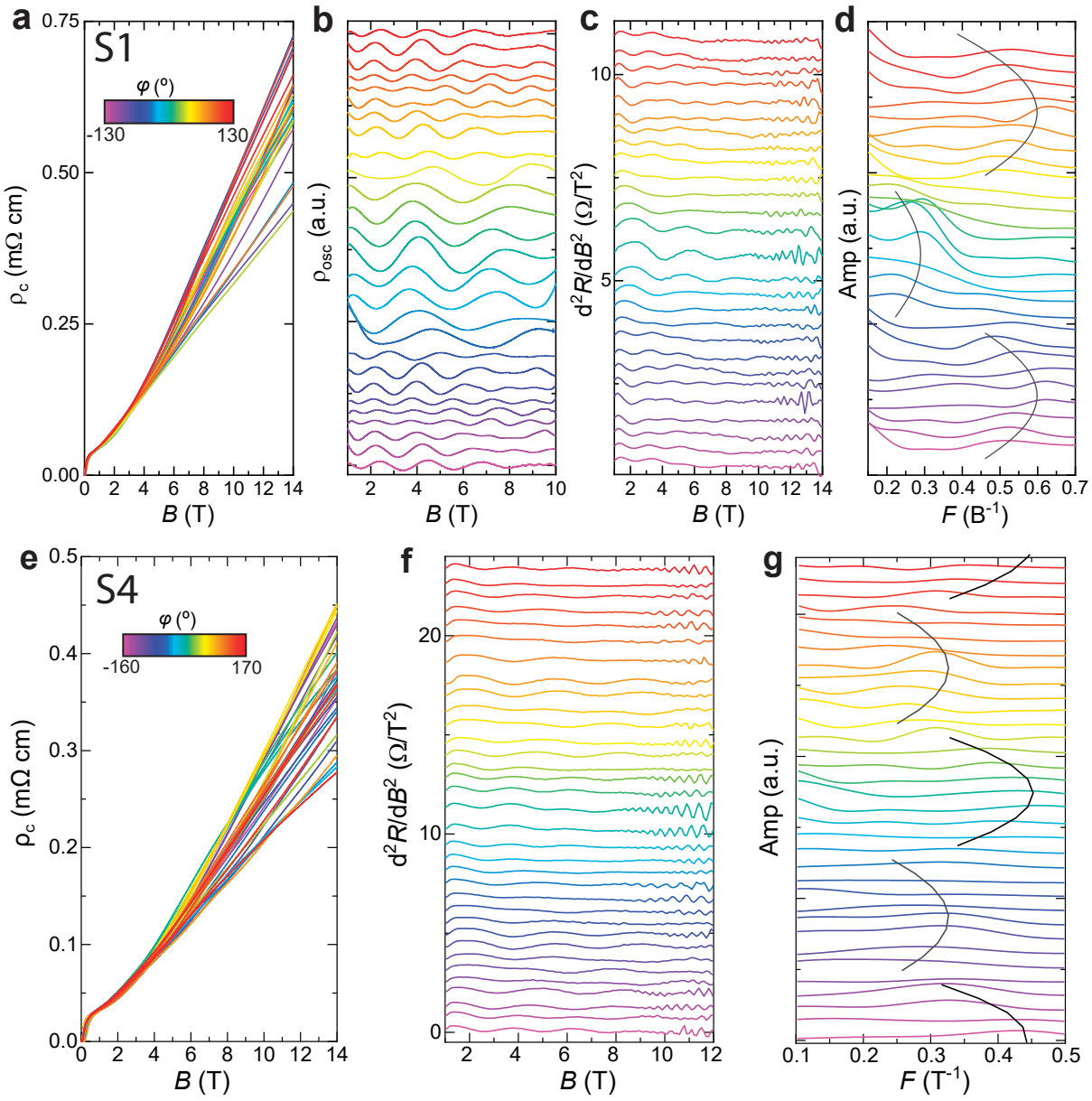

Fig. S 11. **In-plane angle-dependent h/e oscillations of S1 and S4.** (a) Angular dependence of magnetoresistance up to 14T. The measurements are conducted with 10° steps from -130° to 130°. (b) and (c) display the h/e oscillations extracted from polynomial background subtraction and second derivative, respectively. (d) FFT spectrum of h/e oscillations at different angles. The black line indicates the guideline for identified oscillation frequency peaks. (e) Angle-dependent magnetoresistance of S4 measured with a rotation from -160° to 170° in 10° steps. (f) second derivative of magnetoresistance at all angles. (g) FFT spectrum of the oscillations at various angles.

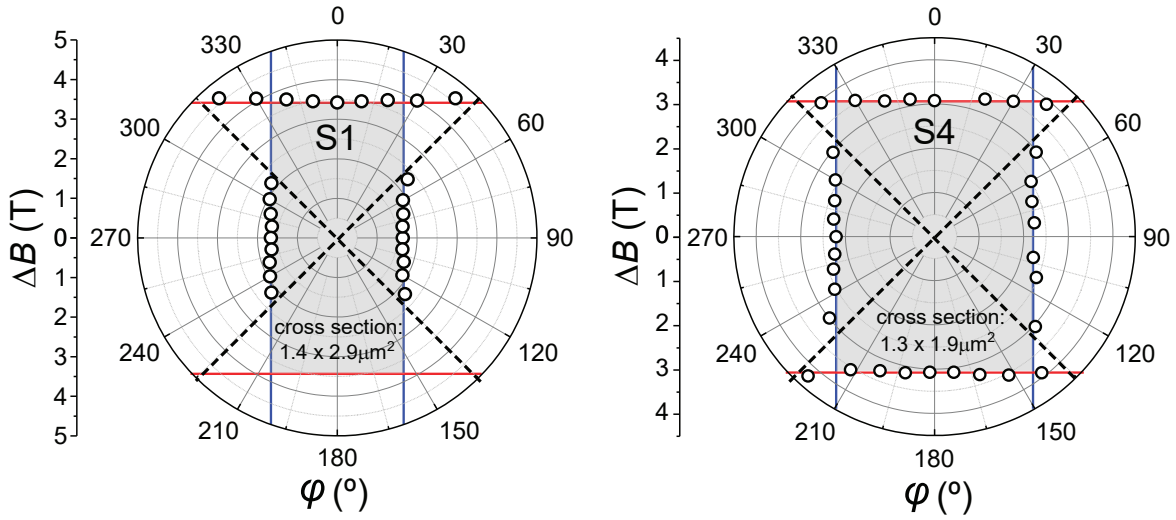

Fig. S 12. **Angular dependence of oscillation periods in device S1 and S4.** Polar plot of oscillation period consistently demonstrates the switching behavior at 45° modulo 90°. The consistent observation of such behavior in two devices of distinct geometries further emphasizes that the switching has no correspondence to the sample geometry.

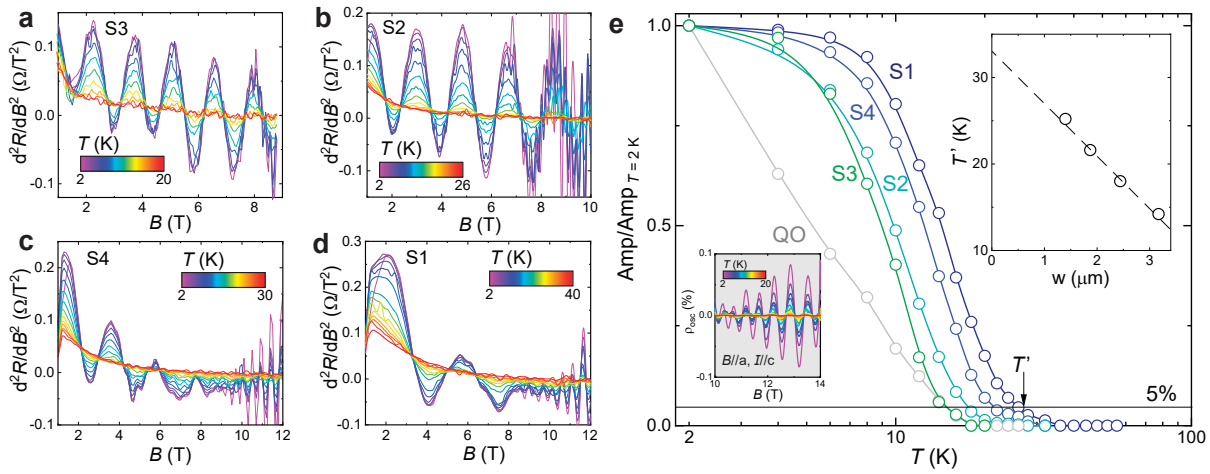

Fig. S 13. **Temperature dependence of h/e oscillation amplitude.** (a)-(d) display the temperature dependence of h/e oscillations in S3, S2, S4, S1, respectively. All measurements are conducted from 2 K to elevated temperatures in 2 K steps. (e) Temperature dependencies of oscillation amplitude across various devices and their comparison to quantum oscillations. The left-hand inset presents the temperature-dependent quantum oscillations measured with current and magnetic fields along the c- and a-direction. The right-hand inset displays the interpolation of T' at zero sample width by linearly extrapolating the temperature where the oscillation amplitude reaches 5% of the value at 2 K. This yields a T' $\approx$ 33 K, which is almost identical to T' determined via other experimental results[2,3].

[1] D. Chen, B. He, M. Yao, Y. Pan, H. Lin, W. Schnelle, Y. Sun, J. Gooth, L. Taillefer, and C. Felser, arXiv:2110.13085 (2021).

[2] C. Guo, C. Putzke, S. Konyzheva, X. Huang, M. Gutierrez-Amigo, I. Errea, D. Chen, M. G. Vergniory, C. Felser, M. H. Fischer, T. Neupert, and P. J. W. Moll, Nature **611**, 461 (2022).

[3] C. Guo, G. Wagner, C. Putzke, D. Chen, K. Wang, L. Zhang, M. Gutierrez-Amigo, I. Errea, M. G. Vergniory, C. Felser, et al., Nature Physics **20**, 579 (2024).

[4] F. H. Yu, T. Wu, Z. Y. Wang, B. Lei, W. Z. Zhuo, J. J. Ying, and X. H. Chen, Phys. Rev. B **104**, L041103 (2021).

[5] C. Guo, A. Alexandradinata, C. Putzke, A. Estry, T. Tu, N. Kumar, F.-R. Fan, S. Zhang, Q. Wu, O. V. Yazyev, et al., Nature Communications **12**, 6213 (2021).

[6] K. Vilkelis, L. Wang, and A. R. Akhmerov, SciPost Physics **15**, 019 (2023).

[7] K. Wang, C. Guo, P. J. Moll, and T. Holder, arXiv preprint arXiv:2409.16088 (2024).

[8] B. R. Ortiz, S. M. Teicher, Y. Hu, J. L. Zuo, P. M. Sarte, E. C. Schueller, A. M. Abeykoon, M. J. Krogstad, S. Rosenkranz, R. Osborn, R. Seshadri, L. Balents, J. He, and S. D. Wilson, Phys. Rev. Lett. **125**, 247002 (2020).